Prediction of sound generated by complex flows at low Mach number regimes

By Y. Khalighi, A. Mani, F. Ham AND P. Moin

1. Motivation and objectives

In many practical applications, sound is generated by interaction of turbulent flow with solid objects. In such cases, sound waves experience multiple reflections from solid objects before they propagate to a far-field point. In these situations the sound spectrum exhibits a rich frequency content consisting of broadband and tonal components. To predict the acoustic field in these situations, a general aero-acoustics framework is required to operate in complex environments. More importantly, the employed method must avoid many simplifying assumptions often made about the geometry, compactness or frequency content of sound sources. The objective of the present work is to develop, validate and demonstrate the functionality of such a computational framework.

The prediction of flow-generated sound requires accounting for the physics of both unsteady flow and sound waves simultaneously. Since these two phenomena exhibit very different energy and length scales, the prediction of flow-generated sound is challenging especially from the numerical perspective. Sound waves carry only a minuscule fraction of flow energy and high-order numerical schemes are required to keep the sound waves intact. Additionally, at low Mach number regimes, the acoustics CFL number imposes extremely small time steps on numerics for resolving both the acoustics and hydrodynamics.

For nearly incompressible flows, Lighthill (1952) formally separated acoustics from hydrodynamics by introducing his acoustics analogy. To predict the far-field sound, Lighthill's analogy is often employed to avoid aforementioned difficulties by designing separate numerics suited for each physical phenomena. At low Mach number regimes, the unsteady hydrodynamics field is computed by an incompressible flow solver in which the time step is not restricted by the acoustic CFL number. The incompressible flow solution is then used to represent sound sources in a separate solver that accurately computes the propagation and scattering of sound waves. By treating the sound waves separately, we avoid large numerical errors that are often present when a compressible solver computes the flow and sound waves simultaneously.

In several studies this method has been applied to predict the sound generated by a trailing-edge flow. Wang & Moin (2000) and Marsden *et al.* (2007) used the incompressible large eddy simulation (LES) technique to simulate the flow over the trailing-edge of an airfoil. To calculate the far-field sound, they simplified the acoustical characteristics of the airfoil by using the acoustics Green's function of a semi-infinite half-plane. To improve the accuracy of the sound calculations, Oberai *et al.* (2002) employed a variational approach to represent the acoustics Green's function of a finite-chord airfoil. However, their approach was designed and applied to flow configurations with homogeneity in the spanwise direction. For engineering applications, many commercial packages such as FLUENT that are designed to simulate flows in general geometry, estimate the far-field sound using a simplified variation of Curle (1955). It is known that such simplification is limited to low-frequency range and cannot capture the broadband components of sound.

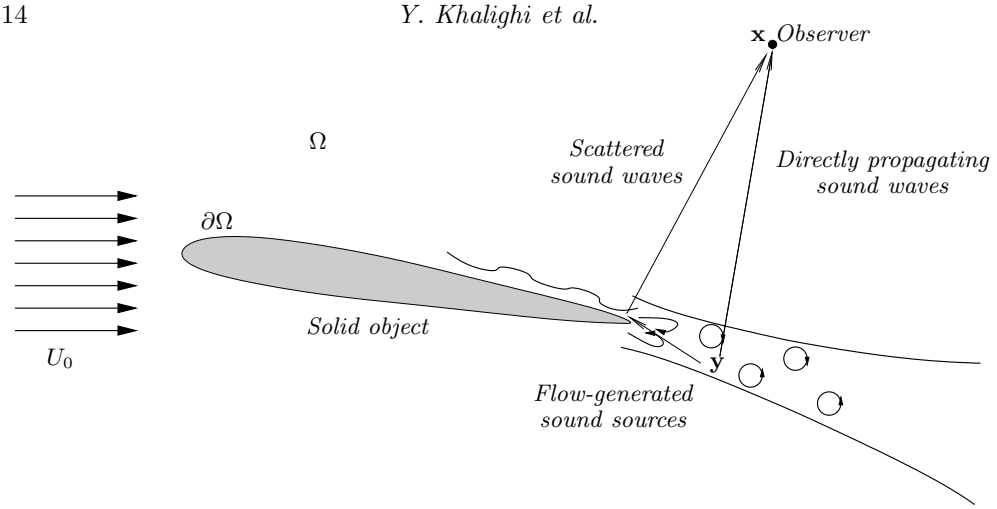

FIGURE 1. Schematic of sound generation and propagation by flow over a generic solid object.

In this work we introduce an aero-acoustics solver that can operate in an arbitrarily complex geometry environment and predict the tonal and broadband components of sound in the entire frequency range resolved by the flow solver. In this *hybrid approach*, the flow-generated sound sources are computed using the unstructured incompressible LES solver of Ham & Iaccarino (2004). These sources are then used as the input to an acoustics solver, where Lighthill's equation is transformed to a boundary integral equation and solved using a specialized boundary element method (BEM) introduced by Khalighi & Bodony (2006). This method does not have any limitations besides the low Mach number assumption and intrinsic limitation of Lighthill's theory described by Crow (1970).

In the following, we first derive the boundary integral equations and introduce the structure of the hybrid approach. Then, we present validation studies of this method for canonical problems of sound generation by laminar and turbulent flows over a cylinder. Finally, we demonstrate the applicability of the method to engineering problems by computing the sound generated by flow around an automotive side-view mirror and provide a detailed comparison with the experimental data.

2. Methodology

2.1. *Derivation of boundary integral equations*

Figure 1 describes the physical setting where acoustic analogy is used. Sound waves are generated by unsteady flow motion and travel to the observer either directly or after multiple reflections from hard walls. Based on this physical picture, Lighthill (1952) rearranged the compressible Navier-Stokes equation as an inhomogeneous wave equation for density ρ with flow quantities as source term

$$\left(\frac{\partial^2}{\partial t^2} - c_0^2 \frac{\partial^2}{\partial x_j \partial x_j}\right) \rho = \frac{\partial^2 T_{ij}}{\partial x_i \partial x_j} \qquad in\ \Omega. \tag{2.1}$$

Equation (2.1) is subject to hard-wall boundary conditions on solid walls ($\partial\Omega$) and Sommerfeld condition in the far-field as

$$\begin{array}{rcll} \mathbf{u}_\perp & = & 0 & \text{on } \partial\Omega \\ \lim_{r\to\infty} r^{(d-1)/2}\left(\frac{\partial\rho}{\partial t}+c_0\frac{\partial\rho}{\partial r}\right) & = & 0 & \textit{in far-field} \end{array} \tag{2.2}$$

In Eqs. (2.1) and (2.2), $\mathbf{u}$ is the velocity, c_0 is the reference speed of sound, r is the distance of sound waves from sound sources and d is the spatial dimension of the problem. T_{ij} is the flow-generated sound sources and can be written in terms of flow quantities as

$$T_{ij} = \rho u_i u_j - e_{ij} + \delta_{ij}\left(p' - c_0^2\rho'\right), \tag{2.3}$$

where e_{ij} is the viscous stress, $p' = p - p_0$ and $\rho' = \rho - \rho_0$. Subscript $(\,)_0$ denotes the reference quantities. We take the time Fourier transform of Eq. (2.1) and write it as a Helmholtz equation

$$\left(\frac{\partial^2}{\partial x_j \partial x_j} + k^2\right) c_0^2\tilde{\rho} = -\frac{\partial^2 \widetilde{T_{ij}}}{\partial x_i \partial x_j} \qquad \textit{in } \Omega, \tag{2.4}$$

where $\tilde{(\,)}$ represents Fourier-transformed quantities and $k = \omega/c_0$ is the wavenumber. We apply Green's second identity to Eq. (2.4) and employ boundary conditions from Eq. (2.2)) to transform the Helmholtz equation to a boundary integral equation

$$\begin{aligned} \alpha(\mathbf{x})\left(\widetilde{p'}(\mathbf{x}) + \frac{\widetilde{\rho u_j} u_j}{d}\right) = &- \int_{\partial\Omega\setminus\{\mathbf{x}\}} \widetilde{p'}(\mathbf{y}) \frac{\partial G(\mathbf{x}|\mathbf{y})}{\partial n_y} ds_y \qquad \leftarrow \textit{scattered} \\ &+ \int_{\Omega\setminus\{\mathbf{x}\}} \widetilde{T_{ij}}(\mathbf{y}) \frac{\partial^2 G(\mathbf{x}|\mathbf{y})}{\partial y_i \partial y_j} d\mathbf{y} \qquad \leftarrow \textit{direct} \\ &+ \int_{\partial\Omega\setminus\{\mathbf{x}\}} \widetilde{e_{ij}} n_i(\mathbf{y}) \frac{\partial G(\mathbf{x}|\mathbf{y})}{\partial y_j} ds_y. \leftarrow \textit{direct (viscous)} \end{aligned} \tag{2.5}$$

In Eq. (2.5), $G(\mathbf{x}|\mathbf{y})$ is the free-space Green's function of Helmholtz equation where $\mathbf{y}$ and $\mathbf{x}$ are the locations of source and observer, respectively. $\alpha(\mathbf{x})$ is a geometrical factor and is defined as

$$\alpha(\mathbf{x}) = \begin{cases} 1 & \mathbf{x} \in \Omega \\ 1/2 & \mathbf{x} \in \partial\Omega \\ 0 & \textit{otherwise} \end{cases}. \tag{2.6}$$

Based on Eq. (2.5), far-field sound has two distinct components: *direct* and *scattered*. These two components are depicted in Fig. 1; the portion of sound waves that travel to the observer without encountering the solid object corresponds to the direct sound, while the sound waves that reflect from the solid objects contribute to the scattered sound. Curle (1955) demonstrated that in low Mach number flows the total sound is dominated by the scattered waves because they exhibit a dipolar behavior in contrast to the direct term that often is in quadrupole form.

Equation (2.5) is an exact rearrangement of fully compressible Navier-Stockes equation. Although the purpose of this rearrangement is to extract pressure $\widetilde{p'}$ which represents acoustic waves in the far-field, the source term T_{ij} is dependent on compressible effects because it includes compressible velocity, density and pressure. In the following we describe how the source term is approximated by incompressible quantities.

In almost all low Mach number, non-heated and non-reactive applications, the nonlinear term $\rho u_i u_j$ in T_{ij} is the major contributor to the sound sources. We approximate

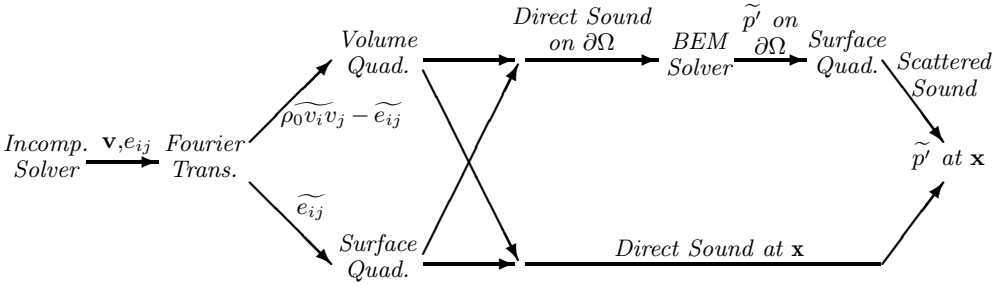

FIGURE 2. Flowchart showing the structure of the hybrid approach.

this term by $\rho_0 v_i v_j$, where $\mathbf{v}$ is taken to be the incompressible velocity field. The adequacy and limitation of this approximation is discussed by Crow (1970). The viscous term e_{ij} is known to be much smaller than the non-linear term and is often neglected; however, Shariff & Wang (2005) demonstrated that viscous shear stress can be an effective source of sound. Therefore we keep this term in the formulation of our hybrid approach. It should be noted that among all of the test cases we studied, the effect of viscosity was only appreciable in the problem of laminar vortex shedding from a cylinder. We neglect the entropic term $p' - c_0^2 \rho'$ because we focus on low Mach number, non-heated and non-reactive flows where the flow can be assumed isentropic.

Having computed the T_{ij} and e_{ij} term using an incompressible solver, pressure $\widetilde{p'}$ remains the only unknown variable in Eq. (2.5). This equation is at the core of the hybrid approach which will be discussed next.

2.2. *Implementation of the hybrid approach*

Figure 2 describes the process of calculating sound at an observer location $\mathbf{x}$ using Eq. (2.5) from an incompressible solution. We use CDP_IF2, an incompressible flow solver, to compute flow-generated sound sources. CDP_IF2 is a second-order, low dissipation, unstructured LES flow solver based on the numerical scheme of Ham & Iaccarino (2004) and implemented within the CDP framework. CDP was developed at Stanford University as a part of the ASC program and was specialized for high quality and large-scale calculations of multi scale/multi physics problems. The code was successfully tested in a variety of applications.

Having computed the unsteady flowfield $\mathbf{v}$, we calculate the Fourier modes of the components of Lighthill's source term, i.e., $\widetilde{\rho_0 v_i v_j}$ and $\widetilde{e_{ij}}$. Then, for each frequency we substitute these terms in Eq. (2.5) and solve it for pressure $\widetilde{p'}$ in a two-step approach:

1. Solving for $\widetilde{p'}$ on $\partial\Omega$: To calculate pressure $\widetilde{p'}$ in Eq. (2.5), a Fredholm's integral equation of the second kind should be solved. Accordingly, we first take the first integral to the l.h.s. of Eq. (2.5), then we discretize the integral by meshing the boundary $\partial\Omega$ and using a second-order surface quadrature rule. We employ the boundary element method (BEM) of Schenck (1968) to form a well-conditioned linear system of equations. To calculate the r.h.s. of this system of equations, we place the observer point $\mathbf{x}$ at the centroid of each facet and evaluate the second and third integrals in Eq. (2.5). This is equivalent to propagating the sound waves directly to the solid surface. To obtain $\widetilde{p'}$ on $\partial\Omega$, this linear system is solved using the parallel direct solver of Li & Demmel (2003) implemented in SuperLU_Dist Package.

2. Integrating for $\widetilde{p'}$ at the observer point x: Having computed pressure $\widetilde{p'}$ on $\partial\Omega$, we

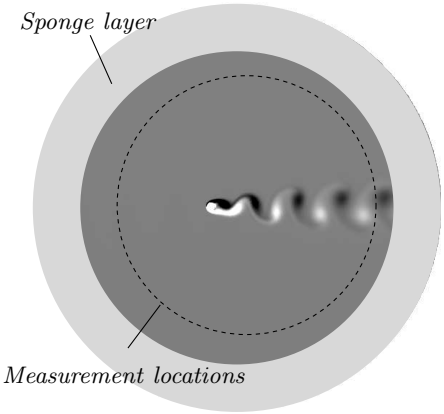

FIGURE 3. Vorticity contour plot of laminar vortex shedding from cylinder at $Re = 100$.

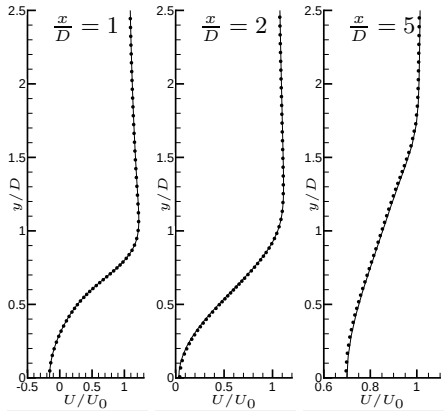

FIGURE 4. U/U_0 for three stations in the wake of the cylinder; ——— , compressible; • , incompressible.

simply use second-order surface and volume quadratures to integrate the r.h.s. of Eq. (2.5) and calculate the total sound at any observer point.

This method does not require any non-reflecting acoustics boundary conditions at far-field in contrast to Finite Element or Finite Volume methods where Dirichlet to Neumann or Perfectly Matched Layer techniques should be employed to avoid reflection of sound waves from exterior boundaries. In addition, by using appropriate free space Green's functions, we can support a variety of acoustics problems such as half-space domains, propagation with uniform background flow and viscous attenuation.

3. Validation

The sound calculated by the hybrid approach is validated against the far-field density fluctuations directly computed using a high-order compressible flow solver. We applied the staggered sixth-order finite difference scheme of Nagarajan *et al.* (2003) and customized it for sound calculation. In particular, a sponge layer was carefully designed to avoid reflection or generation of spurious sound from the exterior boundary.

Since the accuracy of calculated sound closely depends on the flow solution, we study the near-field hydrodynamics in addition to the far-field sound in all of the test cases discussed in this work. Validation studies were carried out for canonical problems of sound generated by laminar and turbulent flow over a cylinder. Identical mesh, run-time and sampling rate were used for both compressible and incompressible simulations.

3.1. *Sound generated by laminar flow over a cylinder*

Laminar vortex shedding from a cylinder at $Re = 100$ and $M = 0.15$ is considered. Computational domain for this flow configuration is shown in Fig. 3. At this Reynolds number, the flow is two dimensional and can be entirely resolved on the computational grid. After achieving periodic steady state, both simulations were advanced for 20 shedding cycles. The Strouhal number of shedding was the same in both simulations and equal to 0.196 which is in agreement with the study of Fey *et al.* (1998). Comparison of mean velocity in Fig. 4 shows excellent agreement of near-field hydrodynamics.

In this flow, the Mach number is small enough to assume the near-field hydrodynamics

is incompressible; however, Inoue & Hatakeyama (2002) concluded that in the propagation of sound to far-field, the effect of background flow should not be neglected. This effect is incorporated by adding a uniform convection term to the Helmholtz equation 2.4 and utilizing the Green's function of that equation in the hybrid approach.

According to Wang *et al.* (1996), silently traveling vortices can generate non-physical sound when they exit the computational domain. To avoid this, velocity field is "silently" damped in a sponge layer shown in Fig. 3; this treatment is applied to both simulations. Additionally, in the compressible simulation the sponge layer absorbs the outgoing acoustics waves and prevents them from being reflected back to the domain.

In the compressible simulation, far-field sound is directly measured by sampling the density signal at measurement locations shown in Fig. 3. Comparison of sound computed from compressible and the hybrid approach is presented in Fig. 5. In this figure the directivity pattern of sound is plotted for the shedding frequency f_{sh} and its first three harmonics. For each frequency, the relative sound pressure level (SPL) is reported in dB. This quantity is defined as

$$SPL = 20log\frac{max(\widetilde{p'})}{max(\widetilde{p'}_0)}, \tag{3.1}$$

where $\widetilde{p'}_0$ is the pressure at shedding frequency.

Figure 5 demonstrates excellent agreement between the directly computed sound and the result of the hybrid approach at the shedding frequency $f = f_{sh}$ and its first harmonic $f = 2f_{sh}$; however, there is a slight difference between the two results at $3f_{sh}$ and significant differences at $4f_{sh}$. In order to understand the root-cause of the observed discrepancy, we used the near-field flow solution from the compressible calculation and evaluated the far-field sound by applying the acoustics analogy of Ffowcs Williams & Hawkings (1969). The difference between computing sound directly and applying an analogy is that by applying the analogy, the propagation of sound waves through the medium is treated analytically; however, in direct computation, wave propagation is prone to numerical errors. In Fig. 5 we observe that the result of the hybrid approach remains almost identical to that of FW-H solution for all frequencies while it deviates from the directly computed sound at high frequencies. At these frequencies, because of the substantially small loudness levels (-52 dB and -80 dB for second and third harmonics, respectively) the magnitude of sound waves are comparable to the size of numerical errors such as dispersion or reflection of waves from the exterior boundaries. This appears to be the case even though our compressible solver is sixth-order accurate in space and second-order accurate in time. As a result, for waves of very small magnitude, the accuracy of directly computed sound is affected by numerical errors, while the hybrid approach is able to predict the sound accurately. In should be emphasized that the dramatic drop in the magnitude of sound waves at high frequencies is caused by the laminar nature of this problem. This drop is not likely to occur in turbulent regimes and as a result the aforementioned numerical errors may not affect the accuracy of directly computed sound in those regimes.

3.2. *Sound generated by turbulent flow over a cylinder*

We consider turbulent flow over a cylinder at $Re = 10,000$ and $M = 0.2$ as the second test case for the validation of the hybrid approach. At this Reynolds number, the flow in the wake is turbulent. Large eddy simulation(LES) with the dynamic model of Germano *et al.* (1991) is employed to account for subgrid scales. The flow is three dimensional and

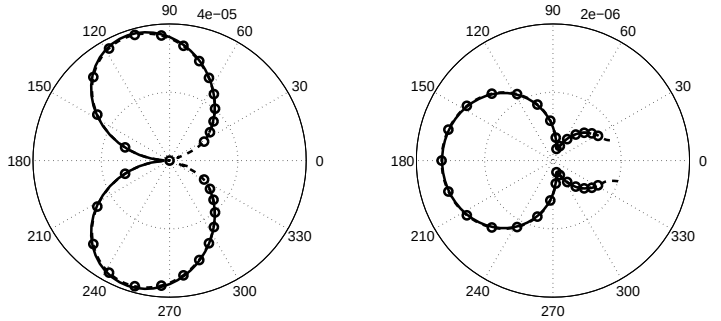

(a) $f = f_{sh}, SPL = 0dB$ (b) $f = 2f_{sh}, SPL = -26dB$

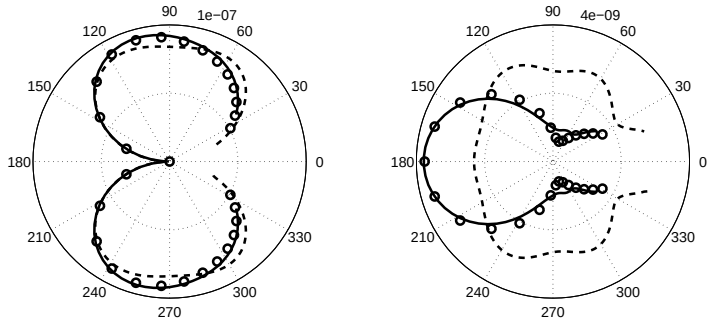

(c) $f = 3f_{sh}, SPL = -52dB$ (d) $f = 4f_{sh}, SPL = -80dB$

FIGURE 5. Directivity plot of sound; ——— , hybrid approach; – – – – , directly computed sound; ∘ , FW-H based on compressible solution.

we used periodic boundary conditions in the spanwise direction for both compressible and incompressible simulations. The spanwise size of computational domain is chosen to be πD, where D is the diameter of the cylinder. After the initial transient phase, both simulations were advanced for 80 shedding cycles. A flow snapshot is shown in Fig. 6. In this picture, obtained from the compressible simulation, the vortical flow structures as well as sound waves are visualized. Clearly, sound waves are mostly generated in the vicinity of the cylinder and their length scale is much larger than the flow length scales.

We compared the near-field hydrodynamics by studying first- and second-order statistics. Mean and r.m.s velocity profiles in the wake of the cylinder are plotted in Fig. 7. These results show good agreement between the compressible and incompressible solutions for low-order statistics. Table 1 summarizes the values of the global flow statistics measured in both simulations in comparison to the results of Dong *et al.* (2006). For validation purposes, we have also provided measures of sampling errors in our results. This is necessary because the turbulent vortex shedding has a slow time scale (order of 10 shedding cycles) and depending on the time window chosen for averaging, the calculated averaged quantity can vary significantly. We quantify the statistical error of an averaged quantity by finding the difference of that quantity averaged in the first half of the sample to that of the second half. The values of uncertainty in few quantities such as ${C_D}^{rms}$ suggest that simulations should be advanced for much longer time to obtain more accurate estimates of these quantities. Considering the statistical uncertainty, the results of Table 1 demonstrate reasonable agreement between compressible and in-

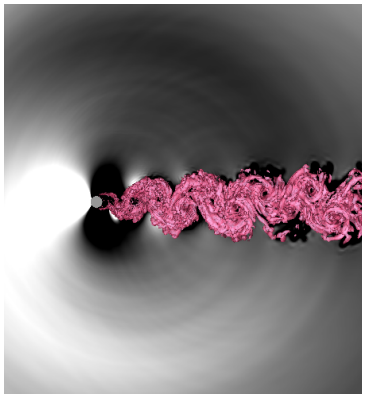

FIGURE 6. Vorticity isosurfaces in color and density contour in grayscale for flow over a cylinder at $Re = 10,000$.

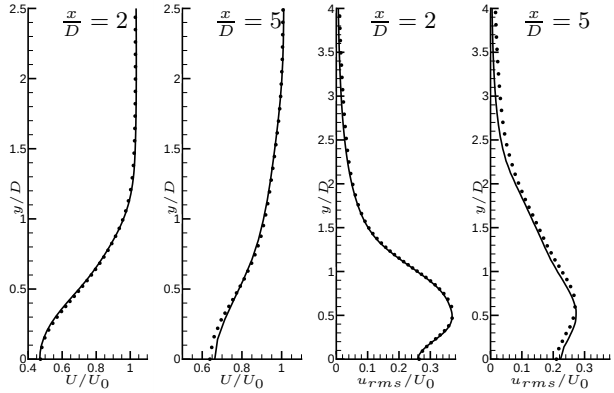

FIGURE 7. U/U_0 and u_{rms}/U_0 for two stations in the wake of the cylinder; ——— , compressible; • , incompressible.

	Incompressible	Compressible	DNS of Dong *et al.* (2006)
St	0.196 ± 0.002	0.192 ± 0.006	0.203
$\overline{C_D}$	1.27 ± 0.03	1.29 ± 0.02	1.143
C_D^{rms}	0.091 ± 0.008	0.098 ± 0.002	-
C_L^{rms}	0.61 ± 0.05	0.63 ± 0.05	0.448
L_c/D	0.69 ± 0.06	0.68 ± 0.01	0.82

TABLE 1. Comparison of shedding frequency St, mean drag coefficient $\overline{C_D}$, r.m.s. drag coefficient C_D^{rms}, r.m.s lift coefficient C_L^{rms} and recirculation length L_c.

compressible calculations. The agreement with the computational results of Dong *et al.* (2006) is marginal.

The crossflow velocity spectrum at a point located 5 diameters downstream of the cylinder on the symmetric plane is shown in Fig. 8. It can be seen that the spectrum of compressible velocity is more energetic at high frequencies. The difference between the numerical methods explains this difference: the sixth-order, staggered numerical scheme of the compressible solver can resolve higher wavenumbers than a second-order, collocated scheme in spite of identical grids.

Sound pressure spectra are compared in Fig. 9 at an observer located approximately 16 diameters above the cylinder. The sound pressure spectra follows the same trend as the velocity spectra. The result of the hybrid approach is in good agreement with the directly computed sound at low and intermediate frequency range while at high frequencies it contains less energy.

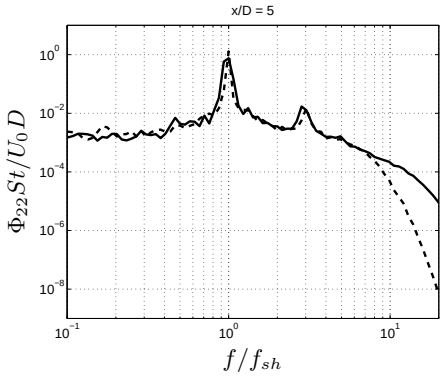

FIGURE 8. Spectral density of crossflow velocity at $(x, y) = (5D, 0)$; ——— , compressible; - - - - , incompressible.

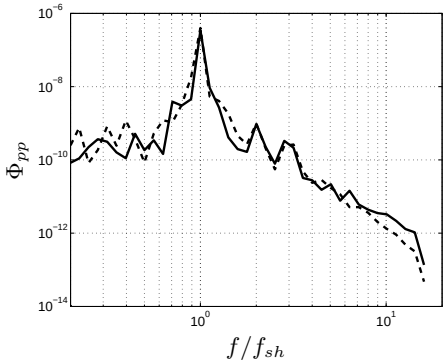

FIGURE 9. Spectral density of sound for an observer located at $(x, y) = (-1.2D, 16.2D)$; ——— , directly computed sound; - - - - , hybrid approach.

4. Sound generated by flow over an automobile side-view mirror

In this section we present the application of the hybrid method to the computation of noise generated by flow over an automobile side-view mirror. Given the freestream velocity of 22.4 m/s (50 mph) and the mirror height of 27 cm, the Reynolds number is approximately equal to 400,000. Experimental measurements for flow over this bluff body, flush mounted on a test table, were conducted at the anechoic chamber facility of the University of Notre Dame and wind tunnel facilities of the Institute for Aerospace Research at National Research Consortium Canada (NRCC). PIV measurements of mean velocity in the wake of the mirror as well as wall pressure spectrum on the body of the mirror and far-field sound spectrum are available for validation of the numerical method.

We used GAMBIT software to generate an unstructured mesh for this flow configuration and the CDP_REFINE tool to homothetically refine the mesh in a zone containing the mirror and its wake. The refined mesh consists of 25 million cells. After the transient flow was convected out of the computational domain, we collected statistics for approximately 0.8 seconds of physical time. This sample size was enough to obtain statistically converged sound spectra with bandwidth of 8 Hz. In terms of computational resources, this simulation required approximately 60,000 CPU hours on 128 Intel Xeon 2.33 GHz processors and 600 GB of disk space.

A velocity snapshot of this flow is shown in Fig. 10. Streamwise velocity contours show that the flow separates from the tip of the mirror; this flow separation then evolves to a turbulent shear layer and forms a recirculation region behind the mirror. Contour plot of wall-normal velocity, shown just above the test table, depicts the footprint of an unsteady vortex filament rolled and bent around the base of the mirror.

Figure 11 shows the comparison of mean velocity to the results of PIV measurements along horizontal and vertical planes cutting through the recirculation region. This result demonstrates that LES is able to accurately predict the size and shape of the recirculation region.

In Fig. 12 wall pressure spectra are plotted against non-dimensionalized frequency at a pressure probe placed at the center of the mirror's flat surface. The non-dimensionalized frequency can be converted to Hz by multiplying by 112 Hz. Simulation result is in agreement with experiment for low and mid-frequency range (up to 1.0 KHz) then it

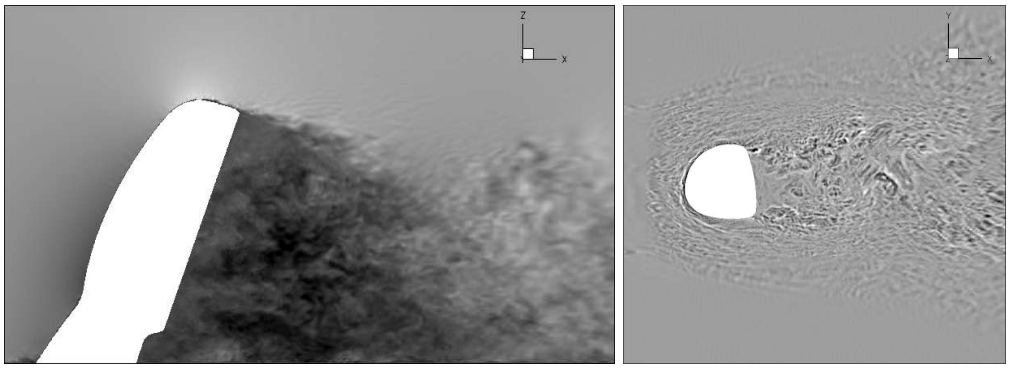

FIGURE 10. Left: Streamwise velocity contours in the midplane of the mirror. Right: Wall-normal velocity contours on a plane parallel and 1 mm above the table.

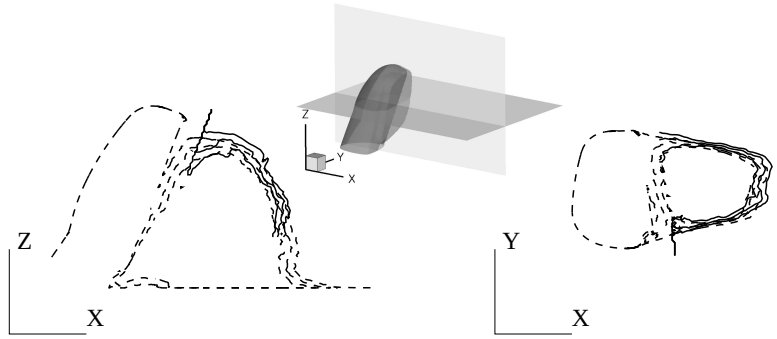

FIGURE 11. Iso-contours of mean velocity on two planes cutting through the recirculation region; contour levels are $U/U_0 = -0.05, 0, 0.05$; ——— , PIV measurements from NRCC; - - - - , LES calculations.

descends rapidly. This cutoff behavior is typical of LES calculations where only energy containing scales corresponding to lower frequencies are resolved.

From an acoustics perspective, the sound waves reflect not only from the mirror but also from the surface of the test table. This effect is included in the hybrid approach by using half-space acoustics Green's functions. The sound spectrum is calculated using the hybrid approach for a microphone located 136 cm away from the mirror and is compared to experimental measurements in Fig. 13. The result of the hybrid approach follows the measured sound in the frequency range of 200 Hz to 1.3 KHz and under-predicts it in the rest of the frequency range. The under-prediction of noise at high frequencies can be due to the limited resolution of sound sources calculated with LES. For low frequencies, one possible reason for the discrepancy is that the tunnel noise (especially fan and motor noise) is overwhelming the sound generated by the mirror.

5. Summary

We developed a hybrid method that consists of an incompressible flow solver and boundary element method (BEM) for accurate prediction of sound generated by complex flows at low Mach numbers.

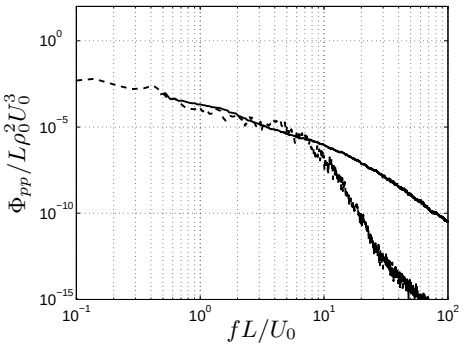

FIGURE 12. Pressure spectral density for a probe located at the flat surface of the mirror; ——— , surface pressure transducer measurement from University of Notre Dame; - - - - , LES calculations.

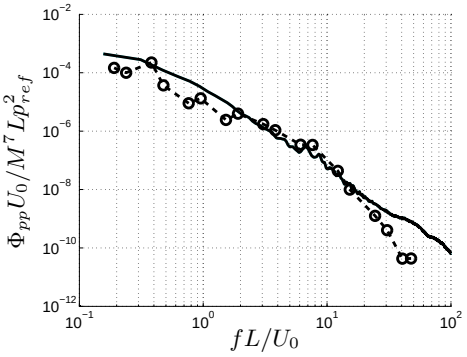

FIGURE 13. Sound pressure spectra at $(x, y, z) = (0cm, 136cm, 0cm)$; ——— , anechoic wind tunnel measurements from University of Notre Dame; —○— , hybrid approach.

This approach was carefully validated for canonical problems of sound generated by laminar and turbulent flows over a cylinder. In laminar vortex shedding, the result of hybrid approach was successfully validated against directly computed sound as well as the result of Ffowcs-Williams and Hawkings acoustics analogy. We demonstrated that the hybrid approach can be even more accurate than the direct computation because it analytically propagates the sound waves and consequently makes the predicted sound less prone to numerical errors. In the case of turbulent flow, we concluded that sound predicted by the hybrid method is as accurate as directly computed sound in the frequency range that the numerical method accurately resolves the flow structures.

As a demonstration of an engineering application, we studied the sound generated by flow over an automobile side-view mirror. The result of the hybrid approach was in good comparison with the experimental measurements in the frequency range adequately resolved by the numerical method.

Acknowledgments

This work was supported by the Office of Naval Research, the U.S. Department of Energy under the Advanced Simulation and Computing (ASC) program, and General Motors corporation. The authors are grateful to G. Iaccarino for providing the computational grid for the side-view mirror case. The authors are also indebted to M. Wang and D. Bodony for their invaluable suggestions during the course of this project. The sound and surface pressure spectra are provided by Hessert lab for aerospace research at University of Notre Dame.

REFERENCES

CROW, S. 1970 Aerodynamic sound generation as a singular perturbation problem. *Stud. Appl. Math* **49**, 21–44.

CURLE, N. 1955 The Influence of Solid Boundaries Upon Aerodynamic Sound. *Royal Society of London Proceedings Series A* **231**, 505–514.

DONG, S., KARNIADAKIS, G., EKMEKCI, A. & ROCKWELL, D. 2006 A combined di-

rect numerical simulation-particel image velocimetry study of turbulent near wake. *Journal of Fluid Mechanics* **569**, 185–207.

Fey, U., König, M. & Eckelmann, H. 1998 A new strouhal–reynolds-number relationship for the circular cylinder in the range $47 < re < 2 \times 10^5$. *Phys. of Fluids* **10** (7), 1547–1549.

Ffowcs Williams, J. E. & Hawkings, D. L. 1969 Sound Generation by Turbulence and Surfaces in Arbitrary Motion. *Royal Society of London Philosophical Transactions Series A* **264**, 321–342.

Germano, M., Piomelli, U., Moin, P. & Cabot., W. 1991 A dynamic subgrid-scale eddy viscosity model. *Phys. of Fluids* **3** (7), 1760–1765.

Ham, F. & Iaccarino, G. 2004 Energy conservation in collocated discretization schemes on unstructured meshes. *CTR Annual Research Briefs,* pp. 3–14.

Inoue, O. & Hatakeyama, N. 2002 Sound generated by a two-dimensional circular cylinder in a uniform flow. *Journal of Fluid Mechanics* **471**, 285–314.

Khalighi, Y. & Bodony, D. 2006 Improved near-wall accuracy for solutions of the helmholtz equation using the boundary element method. *CTR Annual Research Briefs,* pp. 313–322.

Li, X. & Demmel, J. 2003 Superludist: A scalable distributed-memory sparse direct solver for unsymmetric linear systems. *ACM Transactions on Mathematical Software* **29**, 110–140.

Lighthill, M. J. 1952 On Sound Generated Aerodynamically. I. General Theory. *Royal Society of London Proceedings Series A* **211**, 564–587.

Marsden, A. L., Wang, M., Dennis, J. E. & Moin, P. 2007 Trailing-edge noise reduction using derivative-free optimization and large-eddy simulation. *Journal of Fluid Mechanics* **572**, 13–36.

Nagarajan, S., Lele, S. & Ferziger, J. 2003 A robust high-order compact method for large eddy simulation. *Journal of Computational Physics* **191**, 392–419.

Oberai, A. A., Roknaldin, F. & Hughes, T. 2002 Computation of trailing-edge noise due to turbulent flow over an airfoil. *AIAA J.* **40**, 2206–2216.

Schenck, H. A. 1968 Improved Integral Formulation for Acoustic Radiation Problems. *Acoustical Society of America Journal* **44**, 41–58.

Shariff, K. & Wang, M. 2005 A numerical experiment to determine whether surface shear-stress fluctuations are a true sound source. *Phys. of Fluids* **17**, 107105.

Wang, M., Lele, S. & Moin, P. 1996 Computation of quadrupole noise using acoustic analogy. *AIAA J.* **34**, 2247–2254.

Wang, M. & Moin, P. 2000 Computation of trailing-edge flow and noise using large-eddy simulation. *AIAA J.* **38**, 2201–2209.